Characterization of homoclinic chaos through double-valued return time maps

A. R. Zeni,[1] T. Braun,[1] R. R. B. Correia,[1] P. Alcantara, Jr.,[1,2] L. Guidoni,[3,*] and E. Arimondo[3]
[1]*Instituto de Física, Universidade Federal do Rio Grande do Sul, Caixa Postal 15051, 91501-970 Porto Alegre, Rio Grande do Sul, Brazil*
[2]*Departamento de Física, Universidade Federal do Pará, Núcleo Universitário do Guamá, 66075-900 Belém, Pará, Brazil*
[3]*Unitá INFM, Dipartimento di Fisica, Università degli Studi di Pisa, Piazza Torricelli 2, I-56126 Pisa, Italy*
(Received 6 August 1997)

For a laser with a saturable absorber (LSA) and for a subnormal glow discharge (GD), both displaying homoclinic chaos, it is shown that double-valued curves in the return time maps, reconstructed from the time evolution of appropriate variables, are related to different time scales associated with the two mechanisms present in the respective chaotic attractors: the escape from an unstable saddle cycle and the reinjection process. For the LSA the investigation is performed numerically on a 3-2 molecular level model and the results are compared with experimental ones obtained from a CO_2-OsO_4 LSA system having the laser frequency detuning as the control parameter. The analysis is complemented with experimental results from the GD. For both systems we show how to obtain single-valued multibranched return time maps starting from double-valued return time maps, enabling the characterization of homoclinic chaos. [S1063-651X(97)10712-7]

PACS number(s): 05.45.+b, 42.65.Sf, 52.80.Hc

I. INTRODUCTION

In the investigation of nonlinear dynamical systems, the homoclinic orbits have assumed a great importance because their presence is associated with a chaotic behavior. This presence has been examined in several different systems such as (i) the thermokinetics of hydrocarbon oxidation [1], (ii) lasers with electronic feedback [2,3], (iii) lasers with saturable absorbers (LSA's) [4], and (iv) glow discharge (GD) [5]. All these systems display a dynamical configuration determined by a homoclinic orbit to a periodic motion. The connection between homoclinic orbits to a periodic motion and the chaotic behavior has been well established theoretically [6]. A widely employed technique to characterize homoclinic chaos consists in deriving from the chaotic flow in the phase space an associated map. This derivation may be accomplished in several ways and we will denote generically the resulting map as a Poincaré map or return map displaying the features that enables the identification of homoclinic chaos. This technique is not always straightforward, particularly in experimental situations, due to the difficulties of reconstructing a phase space from the variable measured in the experiment. Moreover, some noise is always superimposed on the experimental signal, so that the phase-space reconstruction process may be blown out and the derivation of the dynamical informations from this reconstructed space becomes troublesome.

A secure identification of the presence of homoclinic chaos is obtained when a multibranched return map is derived from the dynamical behavior [7]; the search for that multibranched return map has been performed for the LSA analyses in Refs. [8,9]. An alternative approach to establish the presence of homoclinic chaos is based on the symbolic analysis as applied to the LSA in Refs. [10,11] and for the GD in Ref. [12], with the horseshoe template [13] underlying the dynamics of both the LSA and GD.

Time return maps have been used often as a very suitable method to characterize chaotic dynamics in experimental data series because they may be obtained directly from the measured variable without the need of reconstructing the phase space. Homoclinic chaos consists of a reinjection mechanism connected to an unstable looping behavior. Considering this dynamical configuration, those maps may be classified in two distinct classes: time-of-flight return maps (TFRM's) [8] and return time return maps (RTRM's) [14]. The former are constructed uniquely from the time duration of the reinjection oscillations, whereas the latter use the time duration of all oscillations. In general, TFRM's present single-valued curves, as expected for highly dissipative systems, but depending on how the reinjection phase is identified, double-valued curves may appear. In turn, several recent investigations in the LSA dynamics have shown RTRM's with double-valued structures in different approaches. Theoretical RTRM's with double-valued curves have been constructed from the numerical analysis of the rate equations for the LSA [14]. Experiments using high-resonance absorption in a LSA allowed one to construct RTRM's with double-valued curves directly from the temporal evolution of the laser intensity [15]. These results have led us to associate a homoclinic chaos identification with those double-valued return time maps.

It has been stated in Ref. [8] that in the LSA, as well as in other systems showing homoclinic tangency to a saddle cycle, a TFRM may yield the same information as the Poincaré maps. In this paper the equivalence between a RTRM and a Poincaré map will also be analyzed, but the main purpose of this work is to analyze in more detail the structure of RTRM's with double-valued curves for the dynamics of two nonlinear systems: the LSA and GD. The common feature between these physically different systems is the presence of

*Present address: Laboratoire Kastler-Brossel, École Normale Supérieure, 24 rue Lhomond, Paris Cedex 6, France.

a homoclinic orbit to a saddle cycle, which determines their dynamical evolutions. Our goal is to examine how the sequence of iterations on the maps evolves and which is the mechanism responsible for the double-valued structures. Our analysis starts from the numerical integration of the differential equations for the LSA. We derive RTRM's from the time evolution of the laser intensity for different values of a LSA control parameter and then investigate thoroughly the sequence of the iterations on these maps. The study of these sequences enables us to develop a map model that accounts for the iteration sequences observed in both the LSA and GD. Furthermore, this model suggests that the double-valued maps are obtained when the dynamics of the analyzed systems is an interplay of two separate processes: reinjection and the looping around the saddle cycle, which represent the phase-space evolution associated with the homoclinic orbit to a saddle cycle. As a major result of our work, we have found that exactly the interplay between these two phases leads to the double-valued shape of the maps. The phase space of the LSA and the GD supports our statement that the double-valued curves in the RTRM's are related to how the reinjection and the looping are connected. For both the LSA and GD the shape of the RTRM depends on the choice of the cross section used in the phase space to obtain the map. All cross sections lead to a double-valued structure except one specific cross section, where reinjection and looping are clearly separated and which supports single-valued structures. All the results derived from the numerical analysis for the LSA are confirmed experimentally for both the LSA and GD. Between these systems only a small difference exists, related to the appearance of the double-valued structure, and this difference is also analyzed within the map model. Finally, we show how to obtain single-valued multibranched RTRM's starting from double-valued RTRM's. From a practical point of view, it is desirable to derive the single-valued maps directly from the ''measured'' signal because then we may overcome the noise-associated problem of reconstructing the phase space. The procedure for obtaining single-valued multibranched RTRM's demonstrates how to derive the properties of homoclinic chaos encoded in the double-valued maps.

Section II describes the LSA model and the appearance of chaos in this system. To characterize homoclinic chaos we employ the RTRM's, whose derivation will be analyzed in Sec. III for the simulation and the experimental data on the LSA and for the experimental results for the GD. Because the structure in the RTRM's is related to the sequence of the iterations in the flow dynamics, we have developed an original model that reproduces the observed double-valued RTRM's, as presented in Sec. IV. An analysis of the phase-space dynamics and the related RTRM dynamics is presented in Sec. V for the LSA and the GD. Section VI concludes our work.

II. LSA MODEL AND HOMOCLINIC CHAOS

We use the 3-2 molecular level model coupling both the gain and absorber media for the LSA, introduced by Zambon [16] and analyzed in Ref. [14]:

$$\frac{dI}{dt}=-(-AD+\overline{AD}+1)I,$$

$$\frac{dD}{dt}=\gamma(1-D-DI)-\beta(D+S),$$

$$\frac{dS}{dt}=-\gamma_1(D+S), \tag{1}$$

$$\frac{d\overline{D}}{dt}=-\overline{\gamma}(\overline{D}-1+a\overline{DI}),$$

where I, D, and $\overline{D}$ represent the laser intensity, the population of the laser gain medium, and the population of the absorber medium, respectively; S is an auxiliary variable associated with the pumping mechanism in the amplifier. The parameters A and $\overline{A}$ represent the normalized unsaturable laser gain and absorption, respectively, while a is the relative saturability of the two media. The constants γ, γ_1, and $\overline{\gamma}$ represent the decay rates of the laser variables D, S, and $\overline{D}$, respectively, while β is a coupling constant. The system of equations (1) is dimensionless and the time t is normalized to the cavity decay rate.

Homoclinic chaos is a short term for the complex dynamics that may arise when a system in its phase-space description is near a homoclinic orbit [17]. The LSA homoclinic behavior is evidenced by oscillations on the laser intensity I displaying an alternating periodic-chaotic (APC) sequence, i.e., an alternation between periodic and chaotic patterns both characterized by large- and small-amplitude oscillations. We have simulated this behavior by fixing the LSA parameters to $\overline{A}=1.0$, $a=0.259\,48$, $\gamma=8.0\times10^{-4}$, $\beta=0.099$, $\gamma_1=0.0998$, and $\overline{\gamma}=0.0769$ with the initial conditions $I(0)=42.0$, $D(0)=1.0/43.0$, $S(0)=-1.0/43.0$, and $\overline{D}(0)=1.0/9.5$ and varying the control parameter A. An example of the time evolution for the laser intensity I in the chaotic regime at $A=44$ is shown in Fig. 1(a). Using the notation introduced elsewhere [4], we will denote the regime of periodic oscillations by $P^{(n)}$, where n indicates the number of small-amplitude oscillations following a large-amplitude one. The chaotic signals are denoted by $C^{(n)}$. The transition from $P^{(n)}$ to $C^{(n)}$ occurs through a sequence of period-doubling bifurcations. The $C^{(n)}$ to $P^{(n+1)}$ transition occurs through a tangent bifurcation. The accumulation point of the successive bifurcations corresponds to the homoclinic orbit. The presence of this orbit in the phase space is the key requirement for the occurrence of homoclinic chaos. A homoclinic orbit is an orbit biasymptotic to an invariant set in the phase space for $t\rightarrow\pm\infty$, as a saddle focus or a saddle cycle. In the LSA a saddle cycle is involved. It is not necessary to reach the control parameter values corresponding to a homoclinic orbit in order to observe chaos, and chaotic behavior is expected for parameters close to those of the homoclinic orbit [6].

In the phase-space description of the system of equations (1), there are two fixed points: a saddle node $\mathbf{I}_0=(I_0,D_0,S_0,\overline{D_0})$ and a saddle focus $\mathbf{I}_+=(I_+,D_+,S_+,\overline{D_+})$. Different dynamical configurations are established according to the presence of orbits coupling or not coupling these two

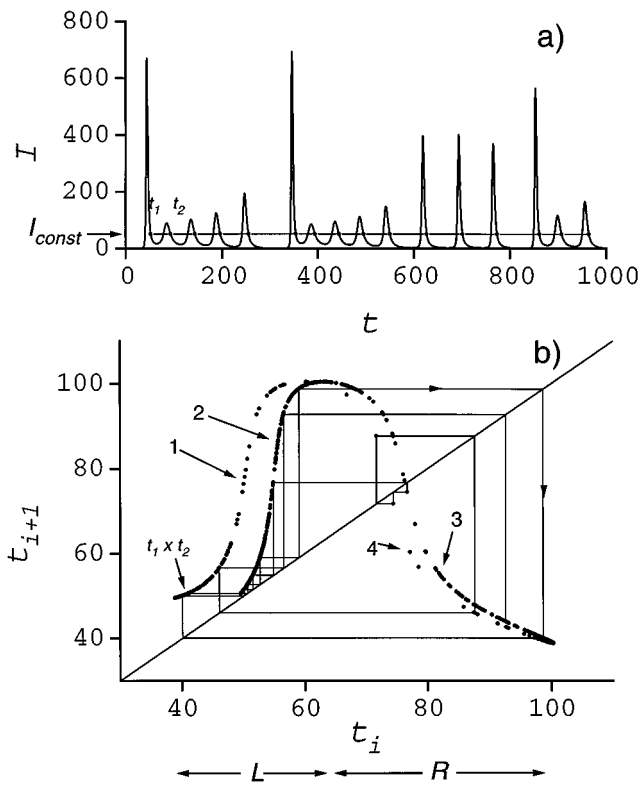

FIG. 1. (a) Temporal evolution of the LSA intensity, derived from the numerical analysis, for the $C^{(5)}$ window at $A=44.0$. The straight line represents the surface $I=I_{const}$. (b) Return time map for the same parameter values with few iterations marked on the map. R and L refer to the symbolic coding used in the text.

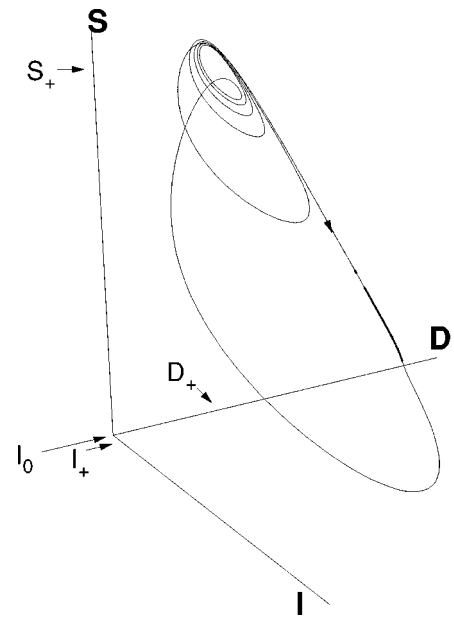

FIG. 2. Excerpt of a $C^{(5)}$ chaotic orbit, projected onto the space (I,D,S), for the LSA model, corresponding to $A=44.0$. The other parameters are the same as in the text. The saddle node at coordinates (I_+,D_+,S_+) is indicated. Only the $I_0=0$ component of the saddle node appears in the figure because $D_0 \simeq 45D_+$ and $S_0 \simeq 45S_+$.

points [9]. For the situation in which the LSA approaches the homoclinic orbit to the saddle cycle, the two fixed points are not coupled and $\mathbf{I}_0$ does not interfere in the dynamics. The LSA parameter values reported previously correspond to these conditions. In Fig. 2 the chaotic orbit corresponding to $A=44.0$ is projected onto the space (I,D,S). We observe that the orbit performs some loops departing with a spiral-type motion from a hole within the phase-space portrait, then moves far from the hole, and finally is reinjected back near it. Therefore, the phase-space dynamics consists of an interplay of an unstable behavior (the spiraling around the hole in the phase-space diagram) and a stable one (the reinjection loop). Both are connected to the phase-space hole, inside of which the saddle cycle is supposed to be present. We have confirmed this presence by locating the cycle with the aid of the procedure developed by Sparrow [18]. Notice that the phase-space hole contains the fixed point $\mathbf{I}_+$ and that all the trajectories remain very far from the fixed point $\mathbf{I}_0$, the $I=I_0$ plane being an invariant surface from which the orbits are repelled [4]. With the change of the control parameter A, the phase-space orbit approaches the orbit homoclinic to this saddle cycle. The dynamical transformations induced by this process are manifested through the APC sequence.

III. RETURN TIME RETURN MAPS

A. Numerical analysis for the LSA

RTRM's may be derived starting from the temporal evolution of the laser intensity I by considering the intersection with the surface of constant intensity that cuts all oscillations, with $I=I_{const}$ and $dI/dt<0$ [19], as shown in Fig. 1(a), and then determining the times t_i between successive intersections. All the derived RTRM's, i.e., the plot t_i vs t_{i+1}, present a double-valued structure. The return map for the chaotic $C^{(5)}$ window at $A=44$ is shown in Fig. 1(b). Due to the crossing of the branches in the top of the double-valued maps (clearly visible in the figure), these double-valued maps are not a proper embedding of the dynamics [20]; still we will show how to use them for the characterization of homoclinic chaos. In Fig. 1(b) we have identified four branches labeled 1, 2, 3, and 4. We consider as the first iteration the one indicated by an arrow on branch 1 of the map [Fig. 1(b)] and the corresponding return times t_1 and t_2 are identified in Fig. 1(a). Branch 1 is related to the first and second loops around the saddle cycle. The iterations associated with the subsequent loops around the cycle fall on branch 2. Therefore, branches 1 and 2 are related to the small oscillations; the first iteration on branch 2 will depend on the position of the previous iteration on branch 1. In other words, branch 2 approaches the bisectrix as much as the iteration on branch 1 allows. Following the iterations associated with the loopings around the saddle cycle, there comes a reinjection loop iteration that always falls on branch 3. The next iteration can fall either on branch 4 or on branch 1. If the orbit makes only one reinjection loop, then the iteration falls on branch 1. Otherwise, after the occurrence of one more reinjection loop, the iteration goes to branch 4. Figure 1(a), between $t=600$ and 800, shows three successive reinjection loops that correspond to a sequence of three iterations on branch 4 before the iteration returning to branch 1. As usual, there is only one loop of reinjection between each set of loops around the saddle cycle; branch 4 is visited much less frequently than the others. The iterations falling on

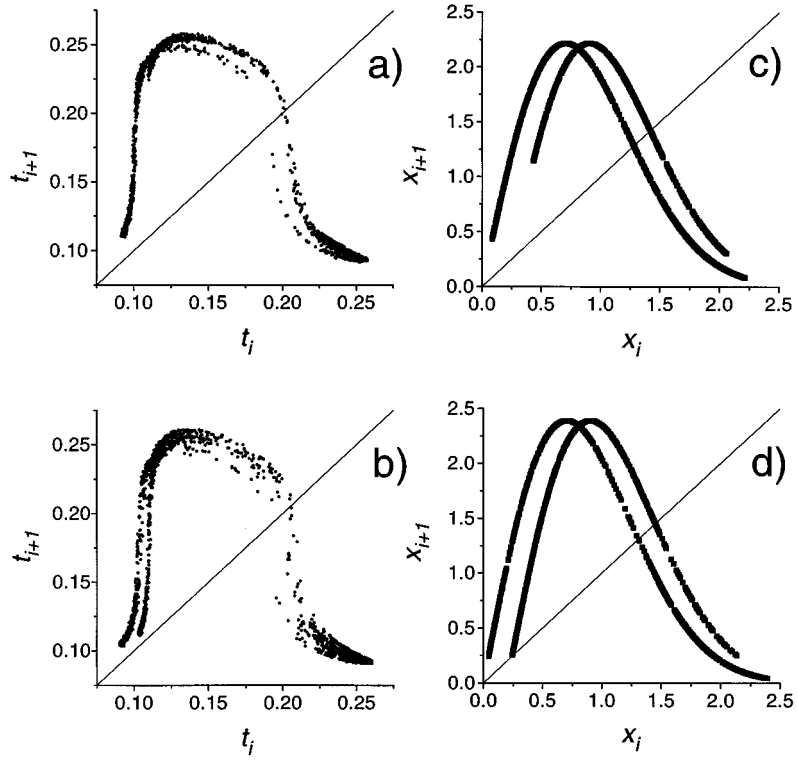

FIG. 3. Return time maps for experimental LSA data at a discharge current of 9.0 mA. (a) $\Delta = -13.4$ MHz, corresponding to the $C^{(2)}$ regime; (b) $\Delta = -14.5$ MHz, corresponding to the $C^{(3)}$ regime. Times are measured in μs. Also shown is the evolution of the map (2) for $c = 0.2$ varying the parameter λ: (c) $\lambda = 1.9$ and (d) $\lambda = 2.05$.

branches 1 and 2 have as abscissas t_i corresponding to a looping around the saddle cycle, while the iterations of branches 3 and 4 have abscissas corresponding to reinjection times.

Looking to the abscissas of the iterations in Fig. 1(b), we may introduce the following symbolic coding. We associate the label L with the two ascending branches (1 and 2) of the return map where the phase-space trajectory loops around the saddle cycle. We associate the label R with the iterations on the descending branches (3 and 4) where the system performs a reinjection. With this coding we can restate the previous description of the iteration sequence. The iterations fall on branch 1 or 4 when the former iteration has an R-labeled abscissa; otherwise the iterations fall on branch 2 or 3. Therefore, branches 1 and 4 are linked together, as are branches 2 and 3.

B. Experimental results for the LSA

The RTRM's for experimental LSA data sets shown in Figs. 3(a) and 3(b) are obtained following the prescription presented previously. The dynamical variable analyzed is the time evolution of the output intensity of a single-mode CO_2 LSA operating on the $10P(12)$ line and containing 225 mTorr of OsO_4 as the molecular gas absorber. As the laser control parameter we used the laser frequency detuning (Δ) modified by piezoelectric ceramics within a range of 90 MHz, which corresponds to one longitudinal mode of the LSA cavity. The laser frequency tuning was measured from the beat note between the output LSA laser field and the output laser field of a waveguide CO_2 laser stabilized upon the Lamb dip of the 4.3-μm fluorescence of the CO_2 molecule. A more detailed description of the experimental setup has been reported elsewhere [15]. At fixed discharge current, by changing only the laser frequency tuning, the time evolution of the laser intensity evolved from the steady state $\mathbf{I}_+$ to the $C^{(n)}$ chaotic regimes. This dynamics has been understood as a homoclinic tangency to a saddle cycle originated from a Hopf bifurcation of $\mathbf{I}_+$ [9]. The maps of Fig. 3 correspond to different chaotic regimes observed at decreasing values of the laser frequency detuning. The map of Fig. 3(a) corresponds to $\Delta = -13.4$ MHz, when the LSA operates in a $C^{(2)}$ window, while at $\Delta = -14.5$ MHz the laser operates in a $C^{(3)}$ window [Fig. 3(b)], the discharge current being fixed at 9.0 mA. The spreading of the points in the transverse direction is associated with the noisy fluctuations intrinsic to the experiment. For both the chaotic $C^{(n)}$ windows, the RTRM's derived from the experimental record for the laser intensity show double-valued structures. The branches on the left part of the map maximum approach the bisectrix of the axes by increasing the n value, i.e., as the system approaches the homoclinic orbit. This behavior is similar to that observed in the LSA numerical simulations, shown in Fig. 1(b).

C. Experimental results for the GD

The GD is a nonlinear dynamical system presenting a dynamics quite similar to that of the LSA; indeed, for both systems the dynamics is modeled by a horseshoe template.

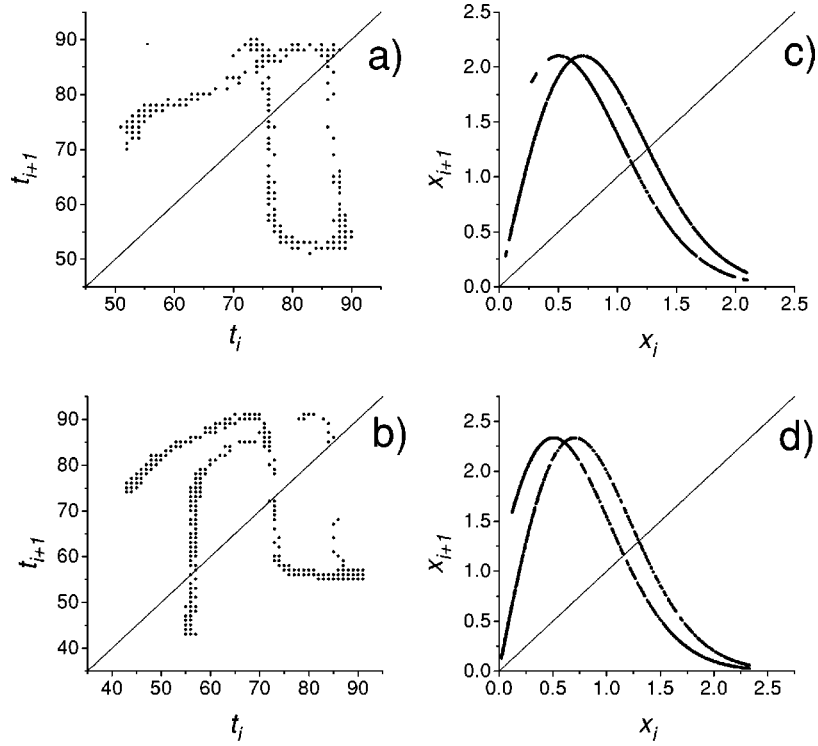

FIG. 4. Return time maps for the GD experimental data corresponding to (a) the $C^{(1)}$ window and (b) the $C^{(2)}$ window. Times are measured in μs. Also shown are maps obtained with the model of Eq. (2) for $c=-0.2$, at (c) $\lambda=1.8$ and (d) $\lambda=2.0$.

The GD, operating in the subnormal regime [21], is fed by a dc voltage source, whose voltage V is the control parameter, while the discharge current I is monitored. Further details of the GD setup have been reported elsewhere [5]. The homoclinic behavior of the GD [22] is demonstrated by self-induced oscillations on the discharge's current displaying the typical APC sequence. Also the sequence of symbols, introduced as in Fig. 1(b), resulting from the iteration of the return map supports the presence of homoclinic chaos. We have constructed GD RTRM's for two chaotic time evolutions corresponding to the $C^{(1)}$ and $C^{(2)}$ windows, respectively, as shown in Figs. 4(a) and 4(b). A double-valued structure is evident in both maps. However, the lengths of the two branches at the left of the map maximum are interchanged with respect to the LSA results, as it appears from a direct comparison between Figs. 3(a) and 3(b) and Figs. 4(a) and 4(b). This indicates that the GD sequence of iterations is different from the LSA one, concerning the order in which the map branches are visited.

IV. MODEL MAP

In order to explore how the sequence of iterations determines the double-valued structure of the RTRM's, we have developed a map model that accounts for the iterations mechanism in both the LSA and GD. We notice that in Fig. 1(b) either branch 1 plus branch 4 or branch 2 plus branch 3 has a bell-shaped appearance that can be described by a particular function $f(x)$, where x represents a return time. Thus the return map seems to be the superposition of two slightly dislocated curves, say, for instance, $f(x)$ and $f(x-y)$. Branches 1 and 4 are described by $f(x)$, while branches 2 and 3 by $f(x-y)$. The jumping from one curve to the other depends on the abscissa x of the iterations. More precisely, let x_i be the abscissa of a generic iteration of the map. If the previous iteration has an abscissa x_{i-1} labeled R, then the ordinate associated to x_i will be given by $f(x_i)$; if x_{i-1} is labeled L, then the ordinate of x_i will be $f(x_i-y)$. This mechanism is described by the model

$$x_{i+1}=f(x_i-y_i), \quad y_{i+1}=c\Theta(x_0-x_i), \tag{2}$$

where $f(x)$ is a ''one-humped'' function, the form of which determines the bifurcation structure of the map when the control parameter is changed. $\Theta(z)$ is the Heaveside step function, which equals 1 when $z>0$ and 0 if $z<0$. The shape of $f(x)$ is not relevant to account for the double structure in the map, and we have chosen $f(x)=\lambda x\exp(1-x^2)$, where λ represents the control parameter. In Eq. (2) x_0 is the point of maximum value for the function $f(x)$ and the value of y_i controls the jumping from one curve to another. To illustrate the properties of our model, the iterations of $f(x)$ for two different control parameter λ at $c=0.2$ are presented in Figs. 3(c) and 3(d). Regarding the double curve structure, they correspond, respectively, to the results of Figs. 3(a) and 3(b). The outcome is that the above model accounts for the same sequence of iterations as observed in both the numerical simulation and the experimental results for the LSA.

A closer inspection of the successive iterations shows that the GD iteration scheme is similar to the LSA one, except that in order to model the GD iterations, we need to replace, in the map of Eq. (2), $f(x_i-y_i)$ by $f(x_i+y_i)$. With this replacement, for different values of the control parameter λ,

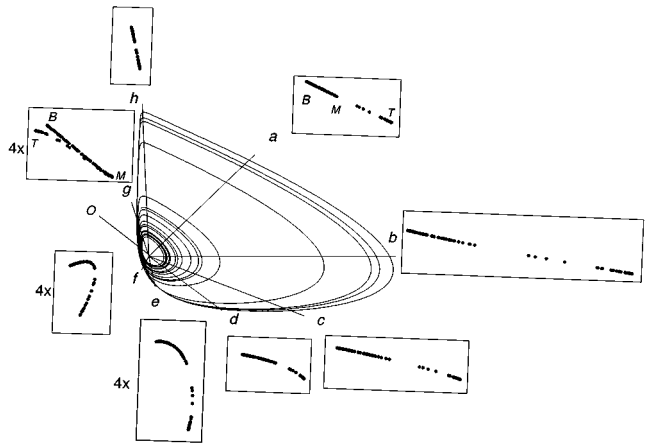

FIG. 5. Projection of the LSA phase space on the (I,D) plane for the temporal evolution of the $C^{(5)}$ window reported in Fig. 1. The lines a–h represent different positions for the section segment. The corresponding intersection points with the flow are shown in the boxes. The letters T and B indicate the attractor's borders and M is the point in the center of the attractor.

the maps of Figs. 4(c) and 4(d) are obtained in close correspondence with those of Figs. 4(a) and 4(b), respectively.

We finish this section with a word of caution about the dimensionality of the map (2). This map is two dimensional in the sense that it cannot be represented by only one function. However, this map dimension is not the dimension of the dynamical system. In effect the dynamical dimension of the LSA and GD systems we have examined is one dimensional because the points on the double-valued return maps scatter along lines.

V. ANALYSIS

A. Phase-space dynamics

The homoclinic chaotic behavior gives rise to a characteristic structure in the dynamical evolution viewed in the associated phase space. This structure is evidenced by the conformation of the strange attractor and, in order to reveal it, we dissect the phase-space dynamics of the LSA in a way similar to that applied for the GD in Ref. [12]. Our topological analysis is implemented in Fig. 5, showing at the center the ID projection onto the ID plane of the attractor corresponding to the $C^{(5)}$ window. The flow is oriented in the clockwise sense. The saddle cycle in the phase-space description originates the hole observed inside the attractor. We consider now the intersections between the LSA flow and a Poincaré section plane rotating clockwise by 2π in the ID plane about the point O inside the hole. When this section plane is fully rotated through the attractor, the successive intersections of the flow with the section plane evidence the stretching and folding mechanisms of the attractor and how the flow is reinjected into itself. The lines in Fig. 5 labeled a–h represent different positions for the cross-section plane. The corresponding intersection points with the flow are shown in the boxes surrounding the projection of the attractor.

Following the notation introduced in Ref. [12], we marked three points in cross section a: T and B are located on the attractor borders whereas M is in the middle. Point B is on the border nearest the saddle cycle, and when the index n of $C^{(n)}$ increases, point B approaches the cycle. After one revolution of the flow, the interval BT is stretched and folded by the flow, resulting in a line segment with a horseshoe shape. This is made clear by comparing the position of points B, M, and T in sections a and g. The associated topological transformation of the attractor's surface is characteristic of homoclinic chaos induced by the creation of a homoclinic tangency of the stable and unstable manifolds of a saddle cycle [12]. The intersection points on the cross sections may be classified according to their position. When they fall within the BM interval, the orbit is looping around the saddle cycle. On the contrary, when the intersections fall within the MT interval, the orbit is in the reinjection phase. According to these two distinct processes of looping and reinjection, we may again codify the dynamics with the symbols L and R; the criterion is whether the flow crosses the intervals BM or MT.

B. Map dynamics

Rather than analyzing the phase-space dynamics in its whole complexity, an associated map provides a simpler method to capture the essential features of the dynamics. From the different ways to obtain a map for a given dynamical system [22], we adopt the standard technique of constructing a map from the intersections of the phase-space

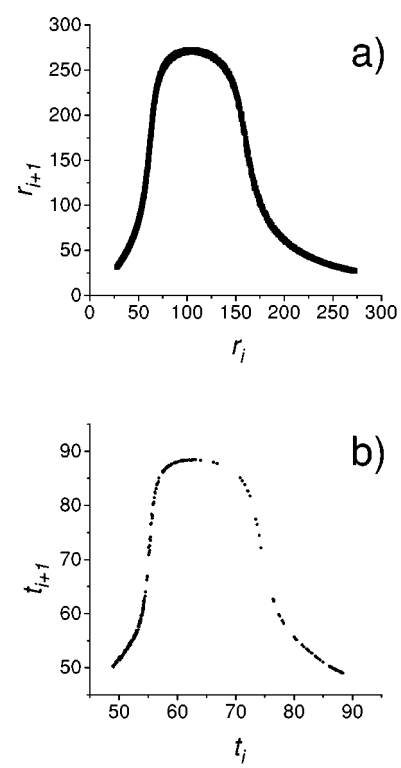

FIG. 6. (a) Poincaré map r_{i+1} vs r_i for the LSA simulation constructed from the intersections of the phase-space flow with the section plane a of Fig. 5. (b) Return time map t_{i+1} vs t_i computed in the phase-space description of the LSA, starting from section g of Fig. 5.

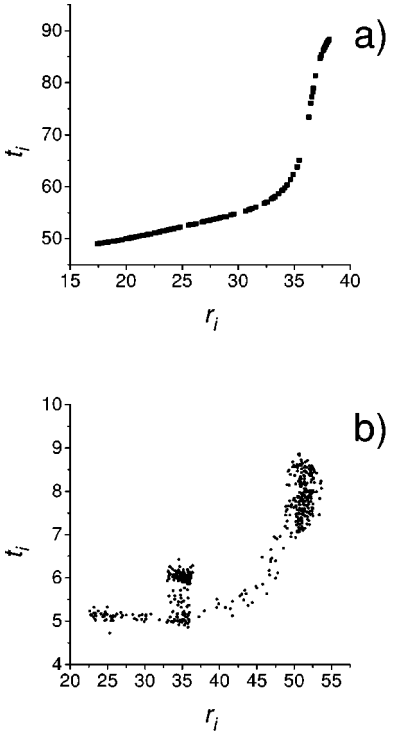

FIG. 7. Return times t_i against the respective starting position r_i on the cross section that yields a single-valued return time for (a) the LSA and (b) the GD. Time is measured in μs.

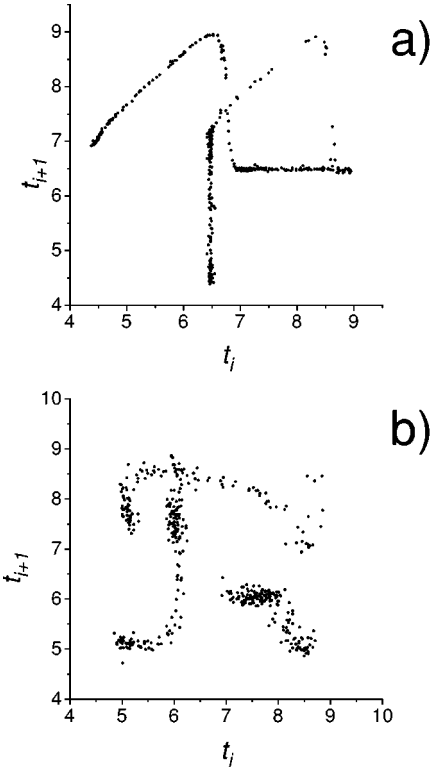

FIG. 8. Return time maps computed in the phase-space description of the GD. The return times were measured (in μs) from a section equivalent to (a) section a of Fig. 5 and (b) section g of Fig. 5.

flow with a section plane. Because of dissipation, the intersections of the flow with the section plane accumulate almost on a one-dimensional manifold, as in Fig. 5. From the various cross sections there, the analysis is straightforward for section a, where the intersection points scatter along a straight line. Parametrizing the position of the intersection points with a distance r along this line ($r=0$ corresponds to $\mathbf{I}_+$), we construct from the successive r_n intersections the Poincaré map r_n vs r_{n+1} of Fig. 6(a). This map presents no double-valued structure. Passing to the map derived from the return time and computing the return times on the basis of the same section a of Fig. 5, we arrive at a double-valued RTRM very similar to that of Fig. 1(b). For other sections, we also obtain double-valued return time maps. However, initiating clockwise from section a, we have noticed that the two branches composing the double-branched structure begin to approach. In terms of the model map of Sec. IV, the curves $f(x)$ and $f(x-y)$ tend to overlap. Thus we have found a special cross section, that denoted by g in Fig. 5, where the return times yields the single-valued map displayed in Fig. 6(b). Such a single-valued map is obtained only for section g. The single-valued one-dimensional maps of Figs. 6(a) and 6(b) are dynamically equivalent because their respective coordinates r and t are related by a monotonic function. In other words, there is a homeomorphism connecting those maps and therefore they yield the same dynamical information. For instance, coding the iterates that fall on the left-hand side of the maps with L and those falling on the right-hand side with R, iterating both maps we obtain the same sequence of symbols L and R. In this sense, both maps give an adequate description of the dynamics of the system.

We now elaborate on the meaning of the cross section from which we obtain a single-valued return time map. For this purpose, for both LSA and GD, we plot the return times t starting from cross section a against the respective starting positions r. The relation between t and r, shown in Figs. 7(a) and 7(b), respectively, for the LSA and the GD is monotonic and composed of two straight segments with different slopes and very similar in shape for both the LSA and GD. Concerning that particular cross section, the monotonic increase of t with r indicates that an orbit evolving on the attractor's outer border has a larger return time than a trajectory moving inside the attractor. This behavior arises because the trajectoy loop has a larger extension when it departs from a larger-r position on the cross section. We verified that trajectories departing from the section with r coordinates contained within the low-slope segment perform a looping around the saddle, while trajectories departing from the high-slope segment execute a reinjection. Therefore, due to the two slopes, we may conclude that the two processes, looping around the saddle and reinjection, have different time scales associated with them. For other cross sections a nonmonotonic and generally double-valued relation between t and r indicates that the times for reinjection and looping are not clearly separated.

We may apply the previous procedure to the GD, as shown in Fig. 8. The GD return time map corresponding to section a of Fig. 1 in Ref. [12] is shown in Fig. 8(a), while Fig. 8(b) shows the GD map for a section of the phase space corresponding to that for the LSA map of Fig. 6(b). The cross section associated with this GD map is located between

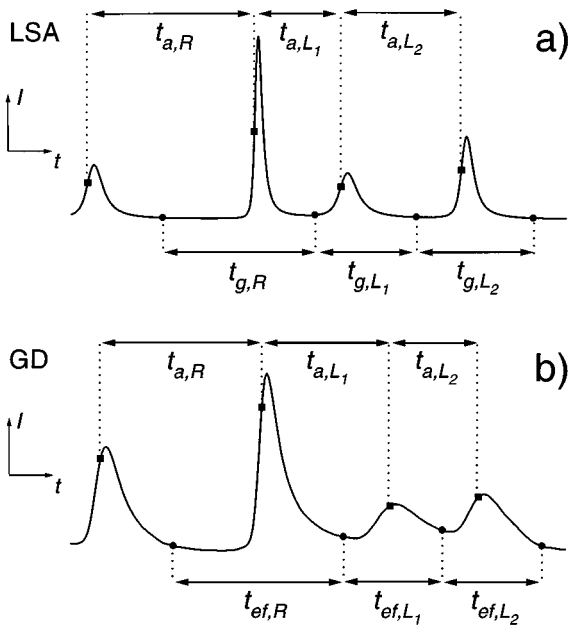

FIG. 9. Temporal evolution of (a) LSA intensity and (b) GD current showing the return times for reinjection and looping computed from two cross sections in the flow. The meaning of the subscripts in the time variables is defined in the text.

sections e and f of Fig. 1 in Ref. [12]. The map of Fig. 8(b) is not exactly single valued, but certainly it does not have the double-valued structure of the map from Fig. 8(a). It is not exactly single valued probably because of the strong influence of noise in the phase-space region where the cross section is applied. In effect, that region is reconstructed mainly from a low-intensity part of the measured signal, therefore with a large noise and a low signal-to-noise ratio. The presence of noise can be detected by the thickness of the map branches.

In order to obtain single-value time return maps it is required to use the proper cross sections of the phase space where the reinjection process begins or where it ends. For the LSA data this happens for section g of Fig. 5. To clarify this point, Fig. 9(a) shows, for the time evolution of the LSA intensity, the return times computed from section g (on the bottom of the figure) and the return times computed from section a (on the top of the figure), with the subscripts g and a identifying the respective cross sections. R refers to the reinjection and L to the looping around the saddle cycle. Due to the key role played by section g, $t_{g,R}$ expresses the ''correct'' duration of the reinjection process, while t_{g,L_1} represents the correct time associated with the first turn around the saddle cycle. For section a the corresponding return times for reinjection and first looping are defined in the top part of Fig. 9(a). From the figure it may be verified that $t_{a,R}>t_{g,R}$ and $t_{a,L_1}<t_{g,L_1}$. This difference arises because of the mixing in section a of the two time scales for reinjection and looping. Such a mixing is visible in the evaluation of t_{a,L_1}, which begins before the end of the reinjection. The reinjection time $t_{a,R}$ is larger than the correct value ($t_{g,R}$) at the expense of the time measured for the first looping after reinjection (t_{a,L_1}), which is then smaller than the correct value t_{g,L_1}. For the return times of the next loopings this difference is not so evident and it may be seen from Fig. 9(a) that $t_{a,L_2}\sim t_{g,L_2}$. For the GD a similar result is shown in Fig. 9(b), with, at the top, the return times computed from section a of Fig. 1 in Ref. [12] and, at the bottom the correct return times obtained from a section located between sections e and f of Fig. 1 in Ref. [12]. The only difference with respect to the LSA case is that for the GD $t_{a,R}<t_{ef,R}$ and $t_{a,L_1}>t_{ef,L_1}$. However, for both the LSA and GD, whenever the flow performs a reinjection, the next return time is modified, and it does not matter whether that return time corresponds to another reinjection or to the first looping around the saddle cycle. In any case, the next return time will be ''shorter'' for the LSA and ''longer'' for the GD. This confirms the choice of the mathematical sign in the map model of Eq. (2): $f(x_i-y_i)$ for the LSA and $f(x_i+y_i)$ for the GD. This analysis confirms that for all cross sections, for instance, a, where we obtain double-valued time return maps, the computation of the return times corresponding to each reinjection and to the next turn (generally a small looping around the saddle, but sometimes another reinjection) is strongly affected by the mixing between the two different time scales.

We may restate the result above by computing the return time $T^{S,S}$ [8] to any cross section of Fig. 5, considered generically as S, as the closed line integral of the reciprocal of the velocity $\vec{G}$ along the orbit $\vec{X}$ departing from $\vec{x_1}$ on S back to S:

$$T^{S,S}=\oint d\vec{X}(\vec{x_1})\frac{\vec{G}(\vec{X}(\vec{x_1}))}{|\vec{G}(\vec{X}(\vec{x_1}))|^2}. \tag{3}$$

Depending on the choice of $\vec{x_1}$, $\vec{X}(\vec{x_1})$ corresponds either to a reinjection loop or to a small looping around the saddle cycle. The different time scales for reinjection and small loopings are responsible for a different behavior of the velocity $G(\vec{X})$: $G_R(\vec{X})$ along the reinjection orbit and $G_L(\vec{X})$ for the loopings around the cycle. We verified that $G_R(\vec{X})>G_L(\vec{X})$ for both the LSA and GD.

Considering now the example of the LSA (a similar result will hold for the GD) we may express the return times corresponding to a reinjection and to the following first small looping, when computed from section g, respectively, as

$$t_{g,R}=T_R^{g,g}=\oint d\vec{X}\frac{\vec{G}_R(\vec{X})}{|\vec{G}_R(\vec{X})|^2} \tag{4}$$

and

$$t_{g,L_1}=T_{L_1}^{g,g}=\oint d\vec{X}\frac{\vec{G}_L(\vec{X})}{|\vec{G}_L(\vec{X})|^2}. \tag{5}$$

For the return times computed from section a we have

$$t_{a,R}=T_R^{a,a}=\int d\vec{X}\frac{\vec{G}_L(\vec{X})}{|\vec{G}_L(\vec{X})|^2}+\int d\vec{X}\frac{\vec{G}_R(\vec{X})}{|\vec{G}_R(\vec{X})|^2} \tag{6}$$

and

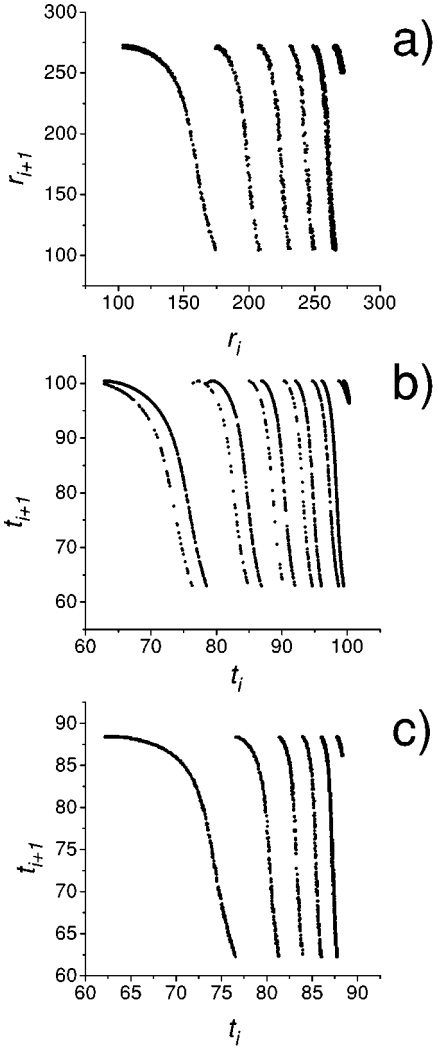

FIG. 10. Multibranched return maps obtained for the LSA from the branch with negative slope in the respective maps of (a) Fig. 6(a), (b) Fig. 1(b), and (c) Fig. 6(b).

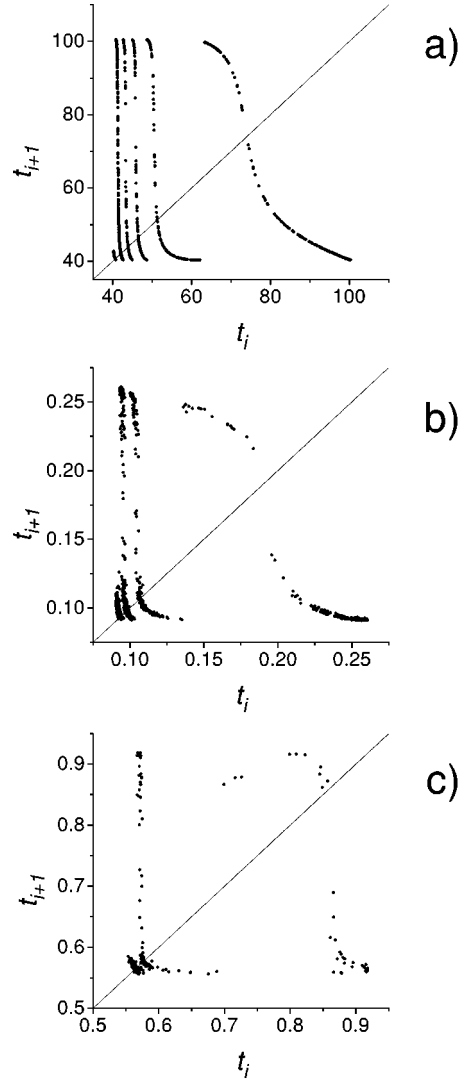

FIG. 11. Single-valued multibranched time return maps obtained for (a) the LSA corresponding to the $C^{(5)}$ window of the numerical analysis of Fig. 1, (b) the experimental LSA data of the $C^{(3)}$ window of Fig. 3(b), and (c) the GD experimental data of Fig. 4(b) corresponding to the $C^{(2)}$ regime. Times are measured in μs in (b) and (c).

$$t_{a,L_1}=T_{L_1}^{a,a}=\int d\vec{X}\frac{\vec{G}_R(\vec{X})}{|\vec{G}_R(\vec{X})|^2}+\int d\vec{X}\frac{\vec{G}_L(\vec{X})}{|\vec{G}_L(\vec{X})|^2}. \qquad (7)$$

The integrals of Eq. (6) are not equivalent to those of Eq. (7) because the paths considered in the integration are distinct in each case. Indeed, in addition to the dependence of the return time on the velocity, $\vec{G}_R(\vec{X})$ or $\vec{G}_L(\vec{X})$, it is important to notice that the computation of the return time in Eqs. (6) and (7) is mainly determined by the path extension. Therefore, the previously mentioned discrepancy in the inequalities (i.e., $t_{a,R}>t_{g,R}$ for the LSA and $t_{a,R}<t_{ef,R}$ for the GD) now may be explained in terms of differences in the path extension for the reinjection and the loopings in the LSA and the GD.

For any cross section other than g a result similar to that for a [Eqs. (6) and (7)] will be obtained. Therefore, in the computation of the return times associated with such section plane, there is a mixing between the reinjection process and the small looping behavior that is not present in the return times computed from section g [Eqs. (4) and (5)]. To sum up, the origin of the double-valued return time return maps obtained for all cross sections except g is explained by this behavior.

In Ref. [8] the equivalence between the return maps for the variable r and the time of flight t was based on the existence of a continuous and invertible functional relation $t=F(r)$ linking these variables. In our case the equivalence between the particular RTRM of section g [Fig. 6(b)] and the standard Poincaré map of section a [Fig. 6(a)] [23] is guaranteed by a monotonic function relating their respective coordinates t and r. This monotonic functional relation exists because there are no foldings in the flow between sections g and a.

C. Multibranched map

Because multibranched return maps represent a secure identification of the presence of homoclinic chaos in a system [8,9], we have examined how to derive those maps from the data presented above. For the LSA numerical analysis, a

multibranched return map is obtained from the map of Fig. 6(a) by retaining only the r_i (the abscissas of the graph) that lie on the branch with negative slope. From them we construct the map r_i vs r_{i+1} displayed in Fig. 10(a). Adopting the same or any similar procedure for the RTRM of Fig. 1(b), we obtain the map of Fig. 10(b). It is obvious that the double-valued structure of the time return map is also present in this multibranched RTRM because each branch is double valued. On the contrary, starting from the single-valued RTRM of Fig. 6(b) and adopting the same procedure, we obtain the single-valued multibranched RTRM shown in Fig. 10(c). However, in order to obtain this last map, it is again necessary to deal with the phase-space representation.

In the derivation of the multibranched RTRM's of Figs. 10(b) and 10(c) only the return times corresponding to the reinjections have been considered. Therefore, these maps are equivalent to the TFRM's derived in Ref. [8]. The reinjection return times are the abscissas of the negative slope branches of the double-valued return time maps. However, because homoclinic chaos properties are encoded not only in the global aspects of the flow (reinjection) but also in local aspects (loopings around the saddle cycle), homoclinic chaos should be characterized not only from the reinjection times but also from the return times following each reinjection. By sampling only the return times following each reinjection we have the advantage that all of them are affected by the mixing process discussed above. Therefore, a map constructed from these return times should not present a double-valued structure. This indeed happens, as may be seen in Fig. 11 for the LSA, (a) in the numerical results, (b) in the experimental results, and (c) for the GD. The multibranched RTRM's of Fig. 11 are slightly different from those of Figs. 10(a) and 10(c). Now the various branches accumulate at the bottom of the left corner, but this has no influence on the symbolic coding necessary for the characterization of homoclinic chaos. The recipe developed above of obtaining single-valued multibranched maps works for return time maps obtained either from the phase-space description or directly from the temporal evolution.

VI. CONCLUSION

Homoclinic chaos for the LSA and GD manifests itself as the connection of two different dynamical mechanisms: the reinjection and the looping around the saddle cycle. The interplay of these two processes determines the properties of homoclinic chaos. These properties may be characterized through maps obtained from the dynamical systems analyzed. We characterized homoclinic chaos from RTRM's obtained directly from the temporal evolution of a dynamical variable (intensity for the LSA, current for the GD) without the need of reconstructing the phase space. Because of the inherent problems associated with the reconstruction of the phase space, return time maps (either RTRM's or TFRM's) could represent the preferable choice to characterize the homoclinic chaos dynamics in experimental data series. These maps often present a double-valued structure, as shown in this paper for the LSA and the GD.

Examining the return times associated with different cross sections in the phase-space flow description of the systems, we have concluded that the double-valued structure of the RTRM's represents an artifact generated by an inadequate choice of the cross section. Owing to such inadequate choice, each return time measured following a reinjection process is improperly sampled and we construct a map on the basis of return times with modified values. We have verified that the inadequate cross section in the phase space gives rise to a double-valued structure in the return maps derived from both the LSA and GD. We have also verified that there is one specific cross section that, on the contrary, yields a single-valued return time map. Within the phase-space evolution, this cross section lies on the border between the mechanisms of reinjection and small loopings. More precisely, this particular cross section better identifies the end of a small looping and the beginning of a reinjection. The dependence of the time return map on the choice of the cross section permits us to establish where in the phase-space flow the reinjection process begins and where it ends.

Both the double-valued RTRM's derived from the temporal evolution of a dynamical variable and the phase-space analysis for the LSA and GD systems have evidenced that for the measured return time each time a reinjection takes place the following return time will be modified. This connection between measured consecutive return times is opposite for the LSA to that for the GD: After a reinjection, the next return time will be shorter for the LSA and longer for the GD. This connection between the successive return times causes the double-valued structure in the RTRM's. In turn, considering the TFRM, an improper determination of the reinjection time gives rise also to a double-valued structure.

The recipe of obtaining single-valued RTRM's and the related multibranched maps directly from the temporal evolution of a dynamical variable requires one to measure the return times starting from a very specific cross section in the phase space. For the LSA and GD experimental data files investigated in this work and in most experimental investigations, the signal-to noise ratio is not large enough to reconstruct the phase space with the required precision. To overcome this problem, we achieved the major contribution of our work: The single-valued multibranched RTRM's have been derived directly from the temporal evolution of the system without dealing with the phase space. The recipe is very simple and easy to implement: It consists in considering only return times following reinjections. These return times are all affected in the same way by the mechanism presented above, and from them a different kind of single-valued multibranched map is constructed. The identification of the multibranched structure, the hallmark of homoclinic chaos, starting from the double-valued map is then possible, even in noisier systems (as a experimental one). In conclusion, single-valued multibranched RTRM's may be derived directly from the temporal evolution of the system without the need to deal with the phase space. Therefore, RTRM's are well suited for the characterization of homoclinic chaos.

ACKNOWLEDGMENTS

A.R.Z., T.B., and P.A. acknowledge support from the Brazilian agencies CNPq, CAPES, and FAPERGS. A.R.Z and P.A. thank M. W. Beims and P. Glorieux for useful discussions. Part of this investigation was performed by P. A. while visiting the Dipartimento di Fisica, Università di Pisa.

[1] P. Gaspard and X.-J. Wang, J. Stat. Phys. **48**, 151 (1987).
[2] F. T. Arecchi, W. Gadomski, A. Lapucci, R. Meucci, H. Mancini, and J. A. Roversi, J. Opt. Soc. Am. B **5**, 1153 (1988).
[3] M. Lefranc and P. Glorieux, Int. J. Bifurcation Chaos **3**, 643 (1993); M. Lefranc, P. Glorieux, F. Papoff, F. Molesti, and E. Arimondo, Phys. Rev. Lett. **73**, 1364 (1994).
[4] F. de Tomasi, D. Hennequin, B. Zambon, and E. Arimondo, J. Opt. Soc. Am. B **6**, 45 (1989).
[5] T. Braun, J. A. Lisboa, and J. A. C. Gallas, Phys. Rev. Lett. **68**, 2770 (1992).
[6] N. K. Gavrilov and L. P. Sil'nikov, Math. USSR Sbornik. **17**, 467 (1972); **19**, 139 (1973).
[7] F. Argoul, A. Arneodo, and P. Richetti, J. Chim. Phys. Phys.-Chim. Biol. **84**, 1367 (1987).
[8] F. Papoff, A. Fioretti, and E. Arimondo Phys. Rev. A **44**, 4639 (1991).
[9] M. Lefranc, D. Hennequin, and D. Dangoisse, J. Opt. Soc. Am. B **8**, 239 (1991).
[10] F. Papoff, A. Fioretti, E. Arimondo, G. B. Mindlin, H. G. Solari, and R. Gilmore, Phys. Rev. Lett. **68**, 1128 (1992); A. Fioretti, F. Molesti, B. Zambon, E. Arimondo, and F. Papoff, Int. J. Bifurcation Chaos **3**, 559 (1993).
[11] H. G. Solari, M. A. Natiello, and M. Vazquez, Phys. Rev. E **54**, 3185 (1996).
[12] T. Braun, R. R. B. Correia, and N. Altman, Phys. Rev. E **51**, 4165 (1995).
[13] N. B. Tuffilaro, T. Abbott, and J. Reilly, *An Experimental Approach to Nonlinear Dynamics and Chaos* (Addison-Wesley, New York, 1992).
[14] A. Zeni, J. A. C. Gallas, A. Fioretti, F. Papoff, B. Zambon, and E. Arimondo, Phys. Lett. A **172**, 247 (1993).
[15] P. Alcantara, Jr., L. Guidoni, A. Barsella, A. Fioretti, and E. Arimondo, J. Opt. Soc. Am. B **12**, 1326 (1995).
[16] B. Zambon, Phys. Rev. A **44**, 688 (1991).
[17] S. Wiggins, *Introduction to Applied Nonlinear Dynamical Systems and Chaos* (Springer-Verlag, New York, 1990).
[18] C. Sparrow, *The Lorenz Equations: Bifurcations, Chaos, and Strange Attractors* (Springer-Verlag, New York, 1982), Appendix E.
[19] The $dI/dt<0$ condition is not a restriction as, using $dI/dt>0$, a similar map is obtained.
[20] T. Sauer, J. A. Yorke, and M. Casdagli, J. Stat. Phys. **65**, 579 (1991).
[21] Y. P. Raizer, *Gas Discharge Physics* (Springer-Verlag, Berlin, 1991).
[22] T. Braun and J. A. Lisboa, Int. J. Bifurcation Chaos **4**, 1483 (1994).
[23] Instead of cross section *a* any other one between *h* and *c* is also a good choice to obtain a Poincaré map similar to that of Fig. 6(a).